Center-to-limb Variations in Solar Plage using IRIS Observations

Pradeep Kayshap[1,2] and Peter R. Young[3,4]

[1]*School of Advanced Sciences and Languages, VIT Bhopal University, Kothrikalan, Sehore Madhya Pradesh - 46611*
[2]*Inter University Centre for Astronomy & Astrophysics, Post Bag - 4, Ganeshkhind, Pune-411007, India*
[3]*NASA Goddard Space Flight Center, Greenbelt, MD 20771, USA*
[4]*Department of Mathematics, Physics and Electrical Engineering, Northumbria University, Newcastle upon Tyne, UK*

ABSTRACT

The center-to-limb variations (CLV) of transition region line Gaussian fit parameters in solar plage are reported for the first time. The Si IV 1402.77 Å line observed by Interface Region Imaging Spectrograph (IRIS) is used. The spectral intensity increases linearly from the disk center to the solar limb. Similarly, the non-thermal velocity also increases linearly from 23.6 km s^{-1} (at the disk center) to 30.9 km s^{-1} (at the solar limb). On the other hand, the Doppler velocity decreases from 8.9±1.0 km s^{-1} at the disk center to 0.0 km s^{-1} at the limb. This CLV pattern in solar plages is consistent with the CLV pattern reported in the quiet-Sun (QS). However, the average values of the parameters in the solar plage are significantly higher than in the QS. The intensity and non-thermal velocity increase linearly with the magnetic field at the disk center while the Doppler velocity does not depend on the magnetic field.

Due to the line-of-sight effect, the plasma column depth increases towards the solar limb which leads to a linear increase in the spectral intensity. Further, the increasing plasma column depth towards the solar limb adds more and more unresolved motions, and as a result, the non-thermal velocity increases from the disk center to the solar limb. In the solar plages, the higher plasma density due to the strong magnetic field leads to the higher intensity and non-thermal velocity compared to QS and coronal hole (CH).

Keywords: Solar transition region(1532) — Ultraviolet spectroscopy(2284) — Center to limb observations(1972)

1. INTRODUCTION

Plages are large areas of enhanced chromospheric brightness on the solar surface that correspond to active regions. They have traditionally been identified in visible chromospheric lines, particularly, H-alpha, but are also clearly seen in full-disk images of the ultraviolet 1600 Å and 1700 Å channels of the Atmospheric Imaging Assembly (AIA: Lemen et al. 2012) instrument on the Solar Dynamics Observatory (SDO). Comparison of these images with line-of-sight magnetograms from the Helioseismic and Magnetic Imager (HMI: Scherrer et al. 2012) on SDO readily demonstrates a connection between plage and strong magnetic fields. Plage regions correlate with the location of photospheric faculae that are collections of small magnetic flux tubes. As active regions age and their flux disperses over the solar surface, plages are replaced by enhanced network (Zwaan 1987).

Plages cause the increase in total solar irradiance from minimum to maximum during the solar cycle (Solanki 2002). They remain bright into the solar transition region, and Barczynski et al. (2018) investigated spatial correlations of IRIS emission lines and AIA 1600 Å with the plage magnetic field. Correlation is greatest for the AIA channel and lowest for the Si IV line, likely due to extended loop structures in the transition region line (Barczynski et al. 2018).

Center-to-limb variations (CLV) of Gaussian fit parameters of optically thin emission lines provide diagnostics of physical processes occurring in the solar atmosphere. Mainly, the CLV in the spectroscopic parameters (i.e., intensity, Doppler velocity, non-thermal velocity) of several chromospheric and transition-region spectral lines is studied for the quiet-Sun and coronal hole (e.g., Dere et al. 1984; Erdelyi et al. 1998; Peter 1999; Peter & Judge 1999; Solanki 2002; Rao et al. 2022; Kayshap & Young 2023). The Doppler velocity is almost zero at the solar limb, and the

Table 1. The table provides all the necessary details about 15 plage observations that are utilized in this work.

Sr No.	Date	Start Time	End Time	Xcen, Ycen	μ Range
1.	13 Dec 2014	07:11:06 UT	07:21:34 UT	-164.46", 175.65"	0.946–0.983
2.	14 Dec 2014	09:08:17 UT	09:26:06 UT	81.15", 174.25"	0.958–0.993
3.	15 Dec 2014	06:16:17 UT	06:34:06 UT	275.13", 183.87"	0.903–0.967
4.	16 Dec 2014	06:38:54 UT	06:56:44 UT	483.41", 183.87"	0.790–0.893
5.	18 Dec 2014	07:24:58 UT	07:42:48 UT	803.57", 179.86"	0.0383–0.637
6.	21 Dec 2014	08:35:38 UT	08:53:28 UT	-464.50", -236.08"	0.0785–0.894
7.	12 Feb 2015	11:10:18 UT	11:28:07 UT	670.01", 283.74"	0.0550–0.745
8.	15 Feb 2015	06:24:18 UT	06:42:08 UT	925.44", 248.63"	0.000–0.414
9.	21 Feb 2015	05:29:20 UT	05:47:09 UT	-689.29", -109.94"	0.0607–0.763
10.	23 Feb 2015	15:51:15 UT	16:09:04 UT	-157.89", -24.59"	0.970–0.995
11.	24 Feb 2015	07:09:18 UT	07:27:08 UT	-17.31", -28.04"	0.993–1.0
12.	26 Feb 2015	05:07:31 UT	05:25:21 UT	370.30", -47.82"	0.887–0.945
13.	01 Mar 2015	01:59:18 UT	02:17:08 UT	842.13", -63.49"	0.328–0.592
14.	03 Mar 2015	23:09:18 UT	23:27:08 UT	475.43", 193.38"	0.0787–0.893
15.	08 Mar 2015	09:51:18 UT	10:09:08 UT	949.77", 125.25"	0.000 -0.389

Doppler velocity (i.e., redshift) increases towards the disk center (e.g., Peter & Judge 1999; Kayshap & Young 2023. Here, it should be noted that, on average, all wave and mass motion should cancel out above the solar limb, therefore, the Doppler velocity at the solar limb is zero (e.g., Doscheck et al. (1976); Peter & Judge (1999)). While the non-thermal velocity is maximum at the solar limb and linearly decreases towards the disk center (e.g., Rao et al. 2022; Kayshap & Young 2023). As we know plasma column depth increases as we move toward the solar limb, and more and more unresolved motions are added. Therefore, the non-thermal velocity is maximum at the solar limb. In Kayshap & Young (2023), we presented results for the Si IV 1402.77 Å line for coronal hole and quiet Sun regions. In the present article, we extend this study to plage regions.

2. OBSERVATIONS

Fifteen IRIS datasets obtained over a three month period from December 2014 to March 2015 were used for analysis. The datasets were chosen as they each contain a plage region and spanned a complete range of heliocentric angles, θ, from $\mu = \cos\theta = 0$ (limb) to $\mu = 1$ (disk center). In each case the same raster was used for the observation: 64 slit positions separated by $2''$ yielding an image size of $127'' \times 119''$, and an exposure time at each slit position of 16 s. Here, please note that the IRIS spatial resolution in the Y-direction is $0.167''$ and the spectral resolution is 26 mÅ. The cadence in each observation is 17 s. Table 1 gives the start and stop times of each raster, the raster centers (Xcen, Ycen), and the ranges of μ values spanned by the rasters. Si IV 1402.75 Å was selected for the analysis as this was the line used by Kayshap & Young (2023), and Section 3.1 describes how the spectral line fit parameters were derived. For each dataset, co-temporal and co-aligned images from HMI and AIA were used to define the plage regions within the IRIS rasters, as described in Section 3.2.

3. DATA ANALYSIS

3.1. *Gaussian Fitting*

Usually, the optically thin lines (such as Si IV 1402.75 Å) of solar atmosphere follow Gaussian distribution, and such lines can fit very well with the Gaussian function[1]. However, if the ions do not follow the Maxwellian distribution of velocities then the line shape deviates from the standard Gaussian shape (Dudik et al. (2017)). Please note that the majority of the Si IV line has a Gaussian shape in the used observations. Now, by applying a Gaussian fit to the

---

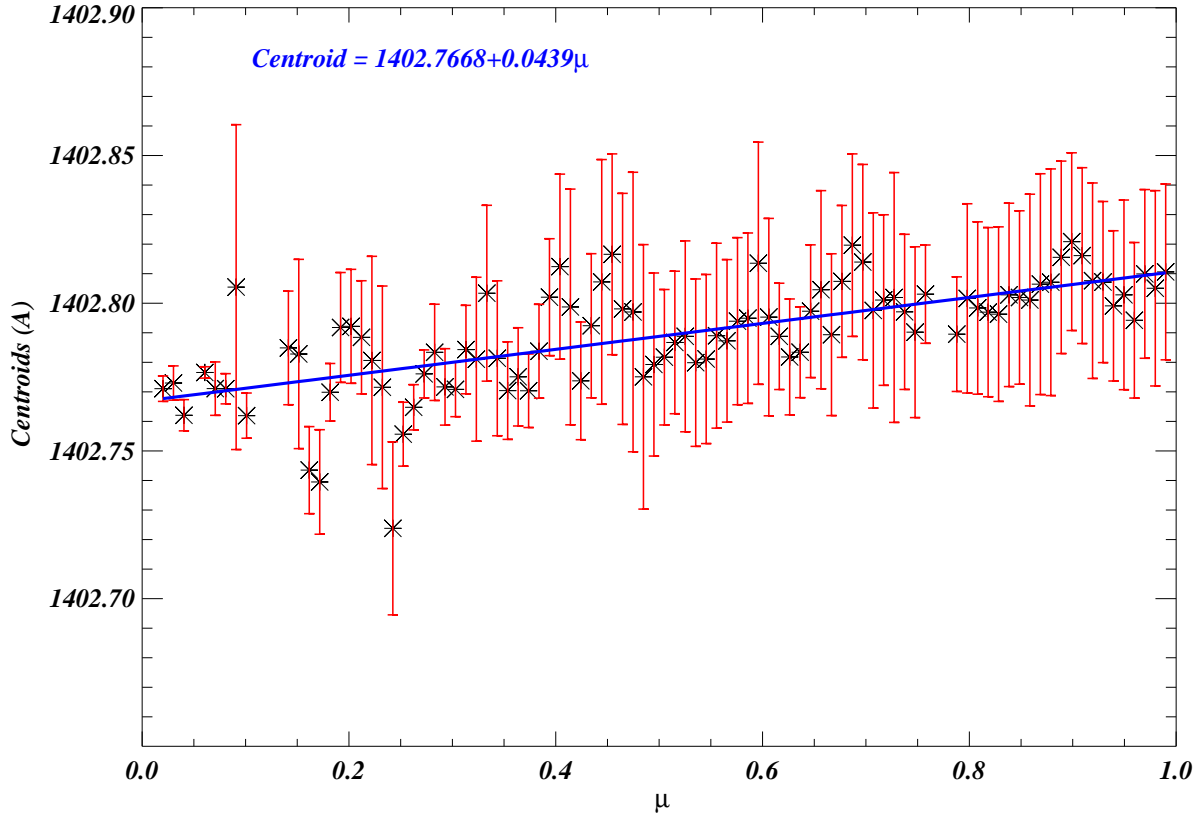[1] https://iris.lmsal.com/itn38/analysis_lines_iris.html

Figure 1. We have created 100 different μ bins from solar limb ($\mu = 0.0$) to solar disk center ($\mu = 1.0$), and then we estimated mean and standard errors of centroid in each μ bin. The mean centroid (from each bin) against the μ bin value is displayed in this figure. The red error bars show the corresponding standard errors. The blue line is the straight line fit, i.e., y = 1402.7668+0.0439μ. Hence, the centroid at the limb is 1402.7668, i.e., the rest wavelength is 1402.77 Å.

observed profiles, we estimate peak intensity (I_p), centroid (λ), and Gaussian width (σ) for each spatial pixel of the IRIS rasters. The I map for dataset 2 is shown in Figure 2(c). To derive Doppler velocities, it is necessary to specify a rest wavelength for the Si IV line. This was obtained by first taking the complete set of centroid measurements and assigning them to 100 μ bins equally spaced between 0 and 1. Figure 1 displays the average centroids in each bin and the errors reflect the standard deviation of the centroids within the bins. A linear fit was performed to the binned centroids (shown on Figure 1), which yields a wavelength of $\lambda_0 = 1402.7668$ Å at the limb. This was used as the rest wavelength for all datasets in order to derive Doppler velocities, v_{D}.

The non-thermal velocity, ξ, is obtained from the full-width at half-maximum (FWHM), w, which is related to σ by $w = 2\sqrt{2\ln 2}\,\sigma$. w can be expressed as a sum in quadrature of three components:

$$w^2 = w_{\mathrm{I}}^2 + w_{\mathrm{T}}^2 + w_{\mathrm{NT}}^2 \tag{1}$$

where w_{I} is the instrumental width (26 mÅ: De Pontieu et al. 2014), w_{T} is the thermal width and w_{NT} is the non-thermal width. The latter two terms are written as

$$w_T^2 + w_{NT}^2 = 4\ln 2 \left(\frac{\lambda_0}{c}\right)^2 \left(\frac{2kT_{\mathrm{i}}}{m} + \xi^2\right) \tag{2}$$

where c is the speed of light, k is the Boltzmann constant, T_{i} is the formation temperature of Si IV (74 000 K is used here), and m is the mass of a silicon ion. The procedure used here is the same as that used by Kayshap & Young (2023) where further details can be found. Maps of v_{D} and ξ obtained from dataset 2 are shown in Figure 2(d) and Figure 2(e), respectively.

Table 2. Linear fit parameters (a, b) and Pearson correlation coefficients (PCC) for I, v_D and ξ.

Parameter	a	b	PCC
$\log I$	1.67 ± 0.033	-0.56 ± 0.058	-0.70
v_D	0.05 ± 0.55	8.89 ± 0.96	$+0.68$
ξ	30.84 ± 0.49	-7.22 ± 0.87	-0.64

3.2. *Selection of Solar Plage Regions*

The precise specification of the plage regions within the IRIS rasters was performed using HMI line-of-sight (LOS) magnetograms, as described below. Datasets 8 and 15 are close to the limb and there is not a good spatial correspondence between the Si IV bright regions and the regions of strong LOS magnetic field. Therefore, for these datasets only, plage was defined using AIA 1600 Å images.

In order to accurately identify the plage regions in the IRIS rasters, it was necessary to first create "pseudo-rasters" from the HMI and AIA image sequences. That is, for each IRIS slit exposure, the nearest-in-time HMI/AIA image was selected and a north-south slit was extracted matching the spatial location of the IRIS slit. As the HMI and AIA plate scales differ from that of IRIS, the slit intensities were interpolated to the IRIS plate scale. The HMI/AIA slits were then assembled to create two-dimensional images that matched the IRIS raster images. The HMI/AIA pseudo-raster images were coaligned to the IRIS intensity maps using the IDL routine get_correl_offsets.pro.

The method for creating pseudo-raster images is illustrated in Figure 2 for dataset 2. Panel (a) shows a representative HMI image of the absolute LOS magnetic field, $|B_\mathrm{los}|$. 64 vertical red lines are over-plotted to indicate the positions of the IRIS slit. Figure 2(b) shows the pseudo-raster image of $|B_\mathrm{los}|$, and Figure 2(c) shows the Si IV 1402.75 Å intensity map for comparison.

The method for identifying plage from HMI LOS magnetograms is derived from the work of Yeo et al. (2013). These authors defined network and faculae (equivalent to plage here) spatial pixels to have a magnetic field greater than three times the local noise level in the magnetogram. The local noise level varies approximately radially across the magnetograms, increasing from 4.9 G at disk center to 8.6 G close to the limb. These results were derived by Yeo et al. (2013) from data obtained in 2010 and we verified them using data from 2014, close to the times of the plage observations. Isolated pixels were excluded from the final plage maps, and only substantially large patches were retained. Figure 2(c)–(e) show the plage contours (blue) overplotted on the I, v_D and ξ maps for dataset 2.

For the observations close to the limb (datasets 8 and 15), pseudo-rasters were created from AIA 1600 Å images and coaligned with the Si IV 1402.75 Å intensity images in the same manner as for the HMI data. An intensity threshold of 110 DN s^{-1} pix^{-1} was applied to the 1600 Å images in order to define the plage regions, and the boundaries were expanded by 5 pixels by applying the IDL dilate.pro function. Figures A.7 and A.14 show the plage boundaries over-plotted on the IRIS line parameter maps for datasets 8 and 15.

4. RESULTS

4.1. *CLV of Spectral Parameters in the Solar Plage*

The procedure described in Section 3.1 was applied to all 15 IRIS datasets to yield I, v_D and ξ at each spatial pixel. The μ value for each pixel was computed based on the spatial coordinates and the HMI pseudo-rasters yielded the B_LOS value for each pixel. The pixels were flagged as plage and non-plage based on the contours derived from the procedure described in Section 3.2.

Taking all of the IRIS plage pixels, 2D histograms of I, v_D and ξ as functions of μ were derived and are plotted in Figure 3. Both I and ξ generally decrease from the limb to disk center, while v_D increases towards disk center. These trends are consistent with coronal hole and quiet Sun results from Kayshap & Young (2023).

An alternative method for displaying the plage data is shown in Figure 4. The data have been separated into 100 μ bins from 0 to 1 in equal intervals of 0.01. For each spatial pixel in a bin, I, v_D and ξ are each averaged and standard errors computed. Figure 4 shows the average values and errors. Linear fits to the three parameters are shown on each plot, and the Pearson correlation coefficients (PCC) between the parameters and μ are given. For v_D and ξ the linear fits obtained by Kayshap & Young (2023) for quiet Sun and coronal hole are over-plotted for comparison. The linear fit parameters, defined as $a + b\mu$, are given in Table 2 with the PCC values.
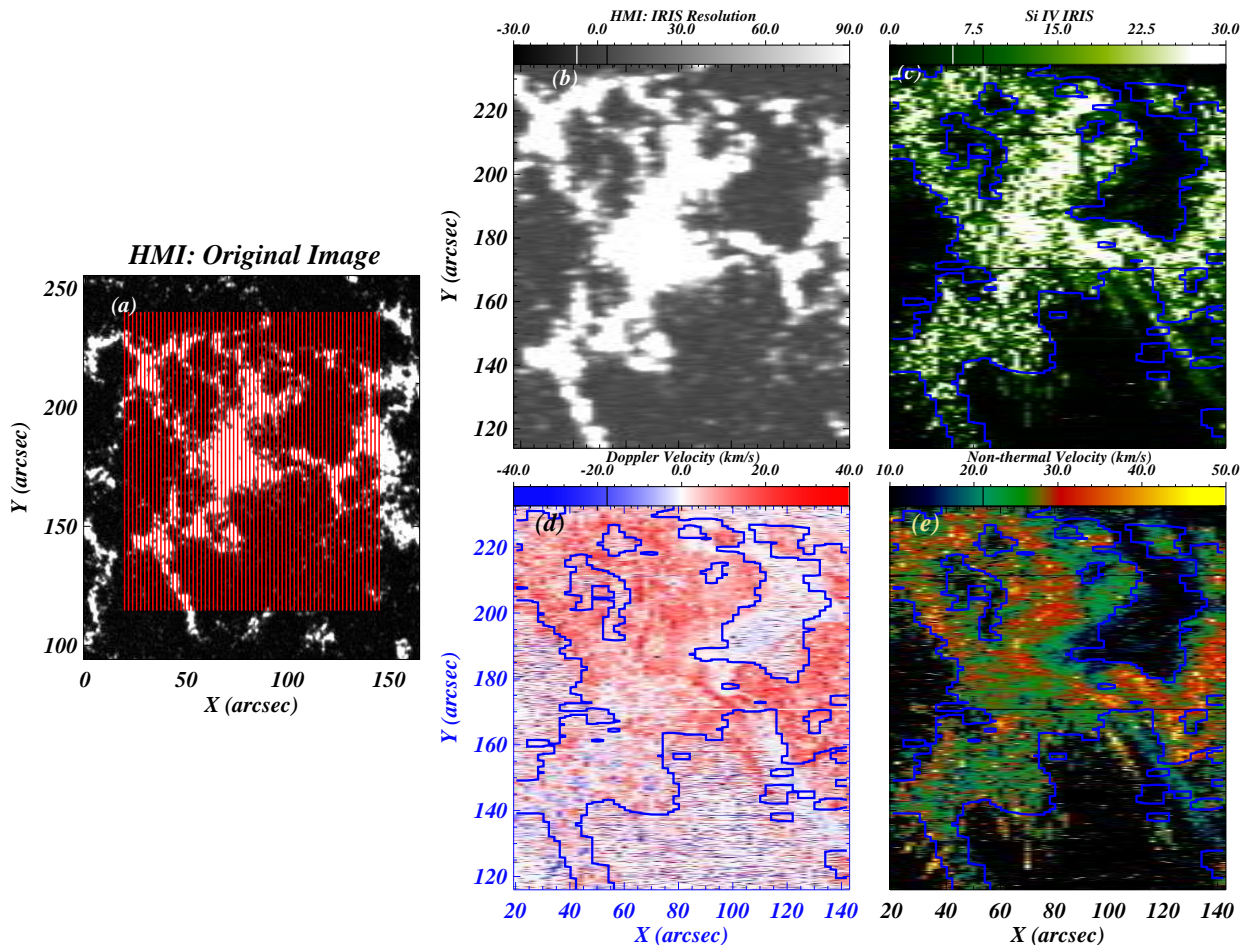
Figure 2. Panel (a) shows the line-of-sight (LOS) photospheric magnetogram (provided by HMI/SDO) from dataset 2 (2014 December 14). The overplotted solid red lines are the 64 slit locations used by IRIS to observe this region. Using the locations from these IRIS slits, we have produced a raster image from the HMI magnetogram corresponding to IRIS observation, which is shown in panel (b). In addition, the panels (c), (d), and (e) show the intensity, Doppler velocity, and non-thermal velocity maps. These maps are deduced by applying a Gaussian fit to the observed Si IV 1393.75 Å line profiles at each location. The overplotted blue contours (in panels (c), (d), and (e)) outline the plage area.

The Doppler velocity at disk center determined from the linear fit is 8.9 km s^{-1}, significantly higher than the values found by Kayshap & Young (2023) for coronal hole and quiet Sun. In addition, the non-thermal velocity is systematically higher in plage by around 5–10 km s^{-1} for all μ values.

4.2. *Variations of Spectral Parameters with the Magnetic Field*

Plage is defined based on the strength of the magnetic field. In this section we investigate whether the average line fit parameters vary with the strength of $|B_{\mathrm{LOS}}|$ within the plage. For this purpose, we consider two IRIS observations close to disk center: datasets 2 and 3 (Table 1). The magnetic field within the plage for these datasets is divided into six bins: 0–50, 50–80, 80–120, 120–200, 200–350, and 350–600 G. The parameters I, v_{D} and ξ are averaged for each bin and the results are plotted in Figure 5 against $<|B_{\mathrm{LOS}}|>$, the mean value of $|B_{\mathrm{LOS}}|$ within the bins. Both I and ξ show increases with magnetic field strength, but v_{D} shows no dependence on B. The variations of the parameters with $\log(<|B_{\mathrm{LOS}}|>)$ are approximately linear, and fits are over-plotted on Figure 5

The green stars on the Panels of Figure 5 are derived from the non-plage regions of the dataset 2 and 3 rasters. For each of the three spectral line parameters, the non-plage values are smaller than the plage values. Whereas the QS intensity is consistent with a linear extrapolation of the plage trend with magnetic field, the ξ and v_{D} QS values are not. The difference for v_{D} is particularly striking and suggests that different physics applies in QS regions compared to the stronger magnetic field plage regions.

5. DISCUSSION AND CONCLUSION

To the best of the authors' knowledge, the CLV of a transition region line's Gaussian line fit parameters has not previously been reported for plage. Here we have used IRIS measurements of the Si IV 1402.77 Å line, which is formed
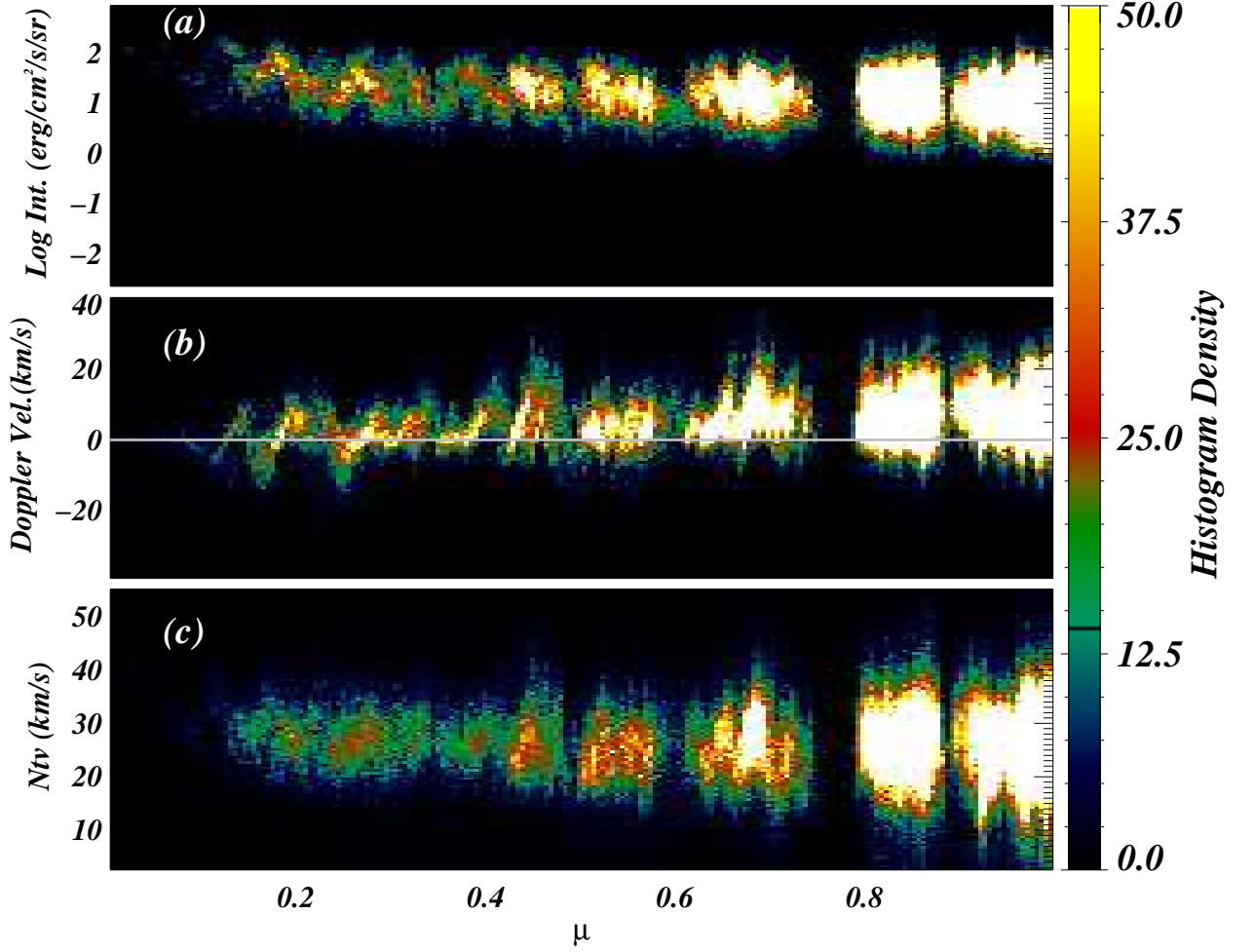
Figure 3. We have displayed the 2-D density distribution of the intensity (top panel), Doppler velocity (middle panel), and non-thermal velocity (bottom panel) with μ. It is clearly visible that intensity and non-thermal velocity are decreasing with μ while the Doppler velocity increases from limb to disk center. The white line in the 2-D Doppler velocity distribution (panel b) shows the zero Doppler velocity.

at a temperature of 80 kK. Fifteen IRIS datasets were chosen to span the range $\mu = 0$ (solar limb) to $\mu = 1$ (disk center). In addition, for the plage datasets close to disk center we have investigated how the line parameters vary with the strength of the magnetic field. The main findings are summarized below, where they are compared with the quiet Sun (QS) and coronal hole (CH) results of Kayshap & Young (2023).

- The intensity, I, has a maximum at the solar limb and log I decreases linearly with μ towards the disk center (Figure 4a).

- The Doppler velocity, v_{D}, is defined to be zero at the limb and increases linearly with μ to a value of 8.9 ± 1.0 km s^{-1} at disk center. The trend matches that for QS and CH but the disk center value is significantly larger than the values of 5.7 and 4.9 km s^{-1} found for these regions (Kayshap & Young 2023). The Doppler velocity signifies the motions that exist in the emitting plasma. Solar plage has a stronger and more complex magnetic field configuration compared to the strength and configuration of the magnetic field of QS and CH. And, the strong and complex magnetic field leads to more dynamics in solar plage compared to QS and CH. This is the most probable reason behind the higher Doppler velocity in solar plage compared to QS and CH.

- The non-thermal velocity, ξ, has a maximum value of 30.9 km s^{-1} at the limb and decreases linearly with μ towards the disk center where it has a value of 23.6 km s^{-1}. The behaviour is again consistent with QS and
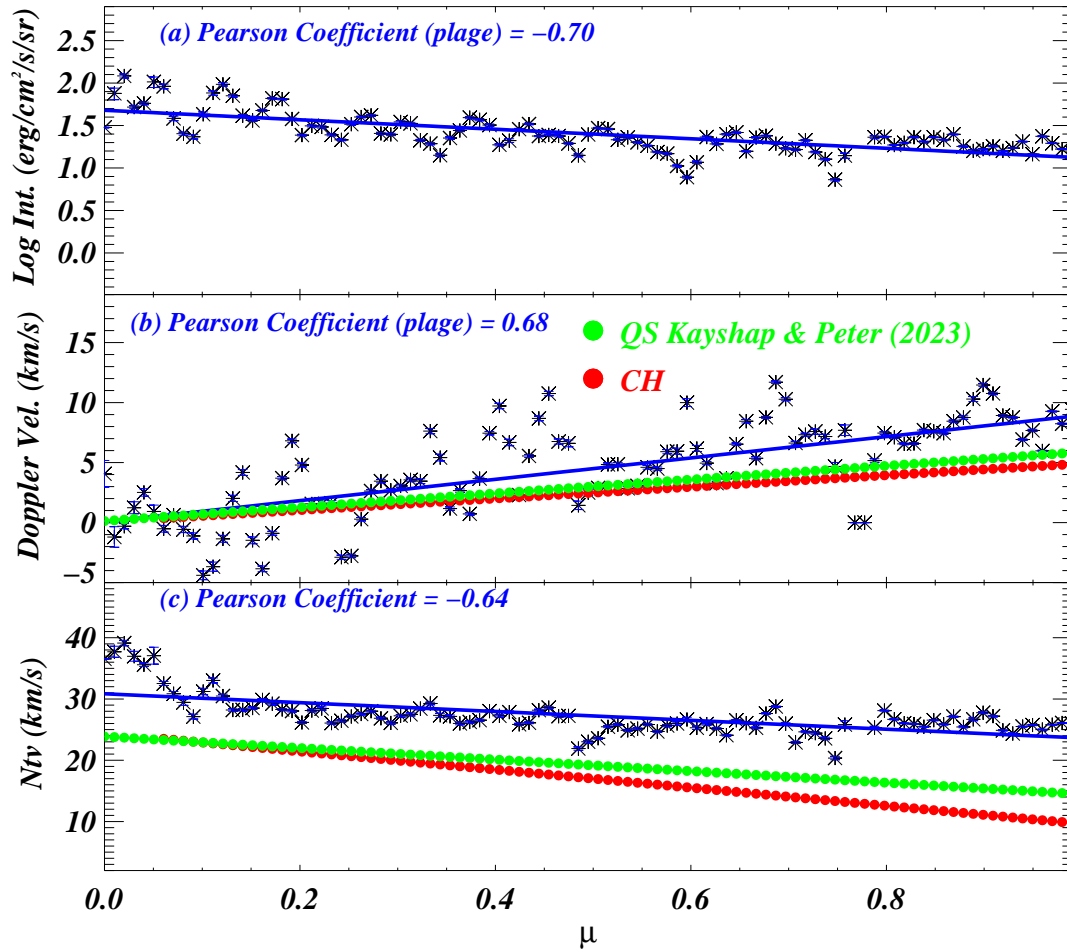
Figure 4. We have calculated the mean and standard error of intensity, Doppler velocity, and non-thermal velocity in different 100μ bins. These 100 μ bins cover the full μ range from 0 (disk center) to 1 (solar limb). This figure displays the variation of mean intensity (top panel), mean Doppler velocity (middle panel), and mean non-thermal velocity (bottom panel) with μ. The blue error bar corresponds to the standard error. The behavior of intensity, Doppler velocity, and non-thermal velocity are similar as we have seen in Figure 3. The blue line in each panel corresponds to the linear fit on the respective parameter of solar plage. Pearson's coefficients for solar plages are also mentioned in each panel. In addition, the green and red dotted lines are the linear fit of the Doppler velocities derived from QS and CH, respectively (panel b). Similarly, we have also displayed non-thermal velocities from QS (green dotted curve) and CH (red dotted curve) in panel (c). The Doppler and non-thermal velocities are taken from Kayshap & Young 2023.

CH, but the values are systematically higher in the plage for all μ values (Figure 4c). At disk center the plage velocity is 9 and 14 km s^{-1} higher than for QS and CH, respectively.

- For plage regions close to disk center, I and ξ were found to increase with the strength of the magnetic field in the plage; $v_{\rm D}$ is independent of the magnetic field strength.

The line intensity increases towards the solar limb due to an increase in the plasma column depth because of the line-of-sight effect. In general, the intensity in plage for the full μ range is higher compared to the QS and CH (Kayshap & Young 2023) which is probably the result of higher density in the plage. In addition, the intensity of the solar plage increases with the magnetic field at $\mu = 1.0$ (near the disk center). This is likely due to plasma density increasing with the magnetic field which leads to the higher intensity. Near the disk center, the Doppler velocity of the solar plage is almost double the Doppler velocity of QS and CH (Figure 4b). The non-thermal velocity is the result of unresolved motions in the in-situ plasma, therefore, the plage regions have more unresolved plasma motions compared to the
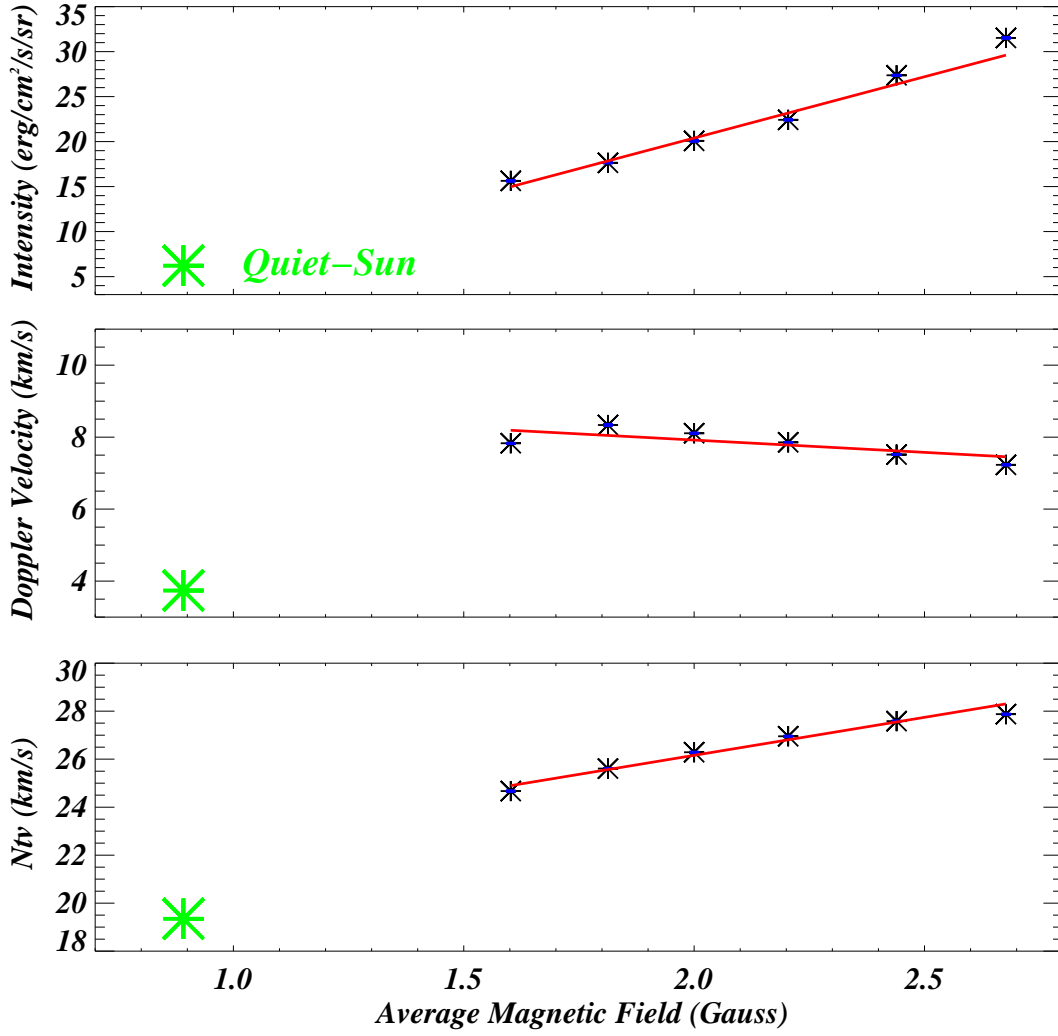
Figure 5. The average of intensity (top panel), Doppler velocity (middle panel), and non-thermal velocity (bottom panel) vs magnetic field. We have averaged over all μ values for each magnetic field bin. The red line in each panel is the linear fit on the corresponding parameter. In addition, we have also displayed the average values of intensity (panel a), Doppler velocity (panel b), and non-thermal velocity (c) by the green asterisk signs from the QS.

QS and CH for all μ values. In addition, the non-thermal velocity increases with the magnetic field (panel c; Figure 5).

REFERENCES

Barczynski, K., Peter, H., Chitta, L. P., Solanki, S. K.,2018, A&A, 619, A5,doi:10.1051/0004-6361/201731650

De Pontieu, B., Title, A. M., Lemen, J. R. et al. 2014,SoPh, 289, 2733,doi:10.1007/s11207-014-0485-y

Dere, K. P., Bartoe, J. -D. F., Brueckner, G. E., 1984, ApJ,281,870,doi:10.1086/162167

Doschek, G. A., Feldman, U., Bohlin, J. D., 1976,ApJL,205,L177,doi:10.1086/182118

Dudik, Jaroslav, Polito, Vanessa, Dzifcakova, Elena, Del Zanna, Giulio, Testa, Paola, 2017, ApJ, 842, 19, doi:10.3847/1538-4357/aa71a8

Erdelyi, R., Doyle, J. G., Perez, M. E., Wilhelm, K.,1998,A&A,337,287

Kayshap, Pradeep, Young, Peter R., 2023, MNRAS,526,383,doi:10.1093/mnras/stad2761

Lemen, J. R., Title, A. M., Akin, D. J., et al. 2012, SoPh, 275, 17. doi:10.1007/s11207-011-9776-8

Peter, H., 1999, ApJ, 516, 490,doi:10.1086/307102

Peter, H.,Judge, P. G., 1999, ApJ,522,1148,doi:10.1086/307672

Rao, Yamini K., Del Zanna, Giulio, Mason, Helen E., 2022, MNRAS,511,1383,doi:10.1093/mnras/stac128

Scherrer, P. H., Schou, J., Bush, R. I., Kosovichev, A. G., Bogart, R. S., et al. 2012, SoPh,275,207,doi:10.1007/s11207-011-9834-2

Solanki, Sami K., 2002, Astronomy and Geophysics, 43, 5.09-5.13,doi:10.1046/j.1468-4004.2002.43509.x

Yeo, K. L., Solanki, S. K., Krivova, N. A., 2013, A&A, 550,A95,doi:10.1051/0004-6361/201220682

Zwaan, Cornelis,ARA&A,25,83,1987,doi:10.1146/annurev.aa.25.090187.000503
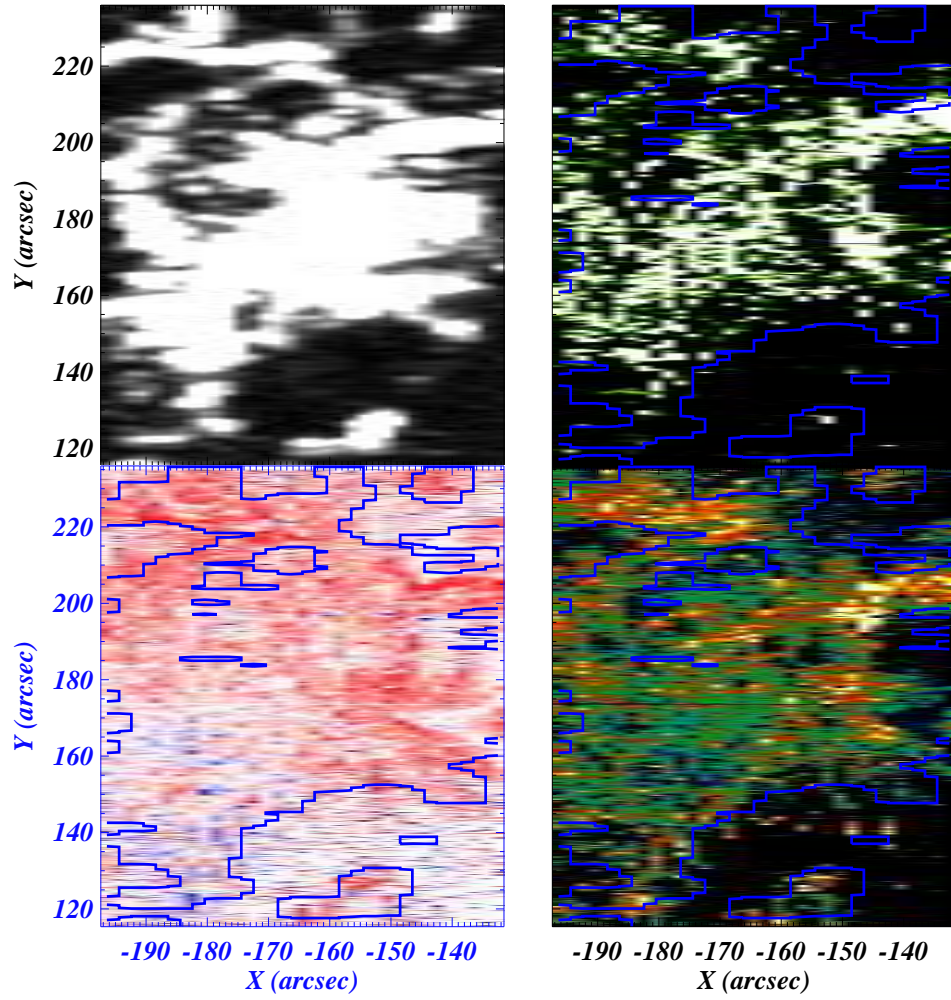
Figure A.1. Same as panels (b), (c), (d), and (e) of Figure 2 but for 13th December, 2014 observation.

APPENDIX

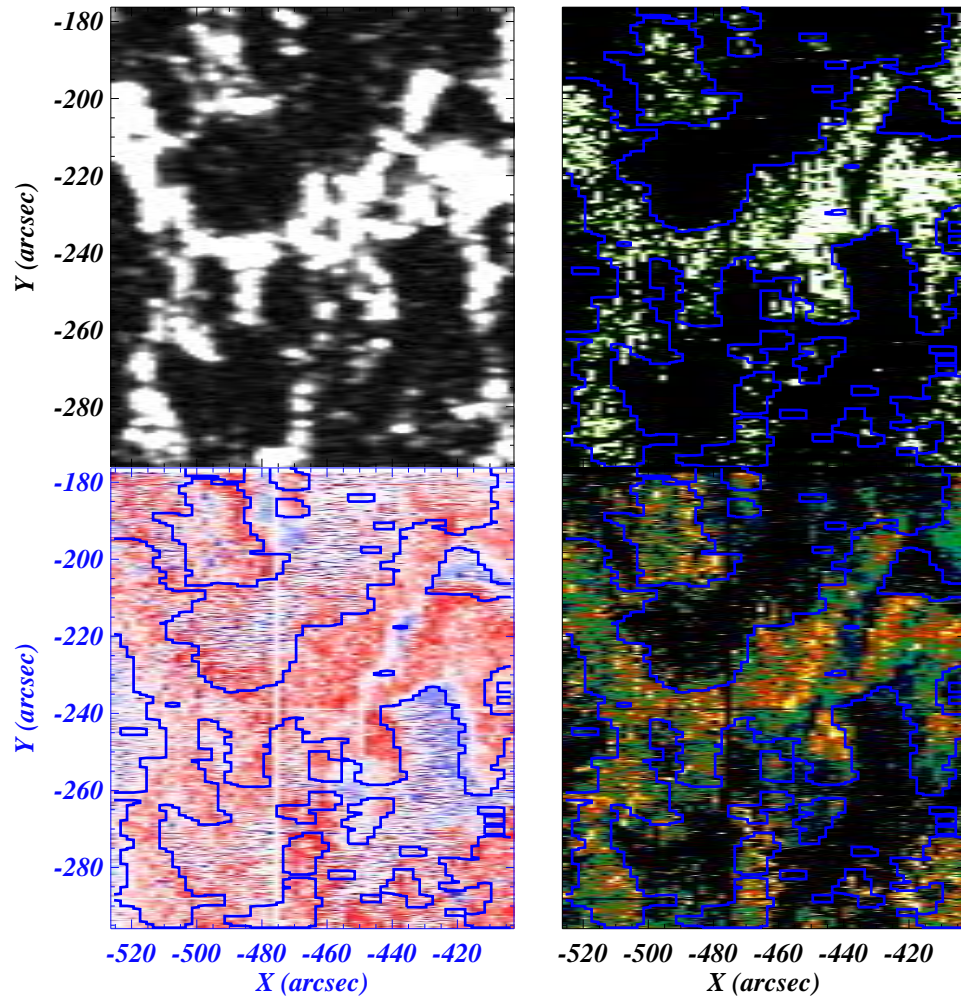A. PLAGES SELECTION IN VARIOUS OBSERVATIONS
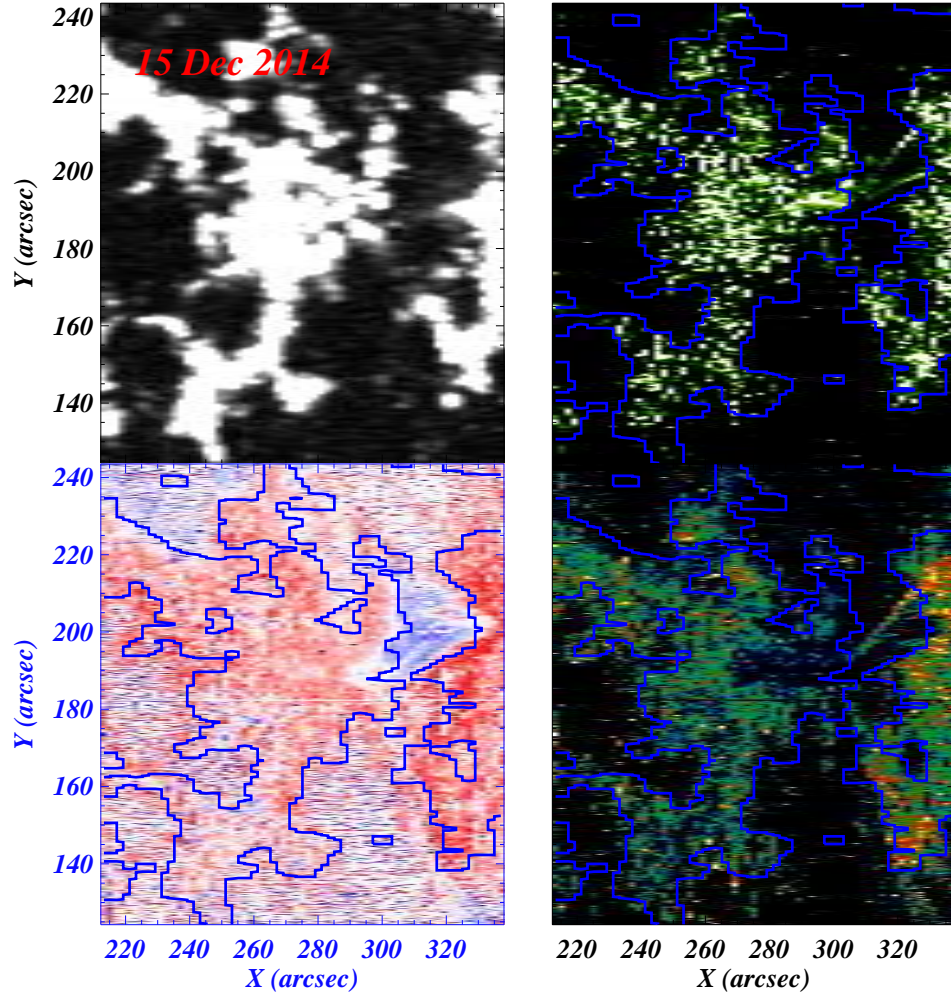
Figure A.2. Same as panels (b), (c), (d), and (e) of Figure 2 but for 15th December, 2014 observation.
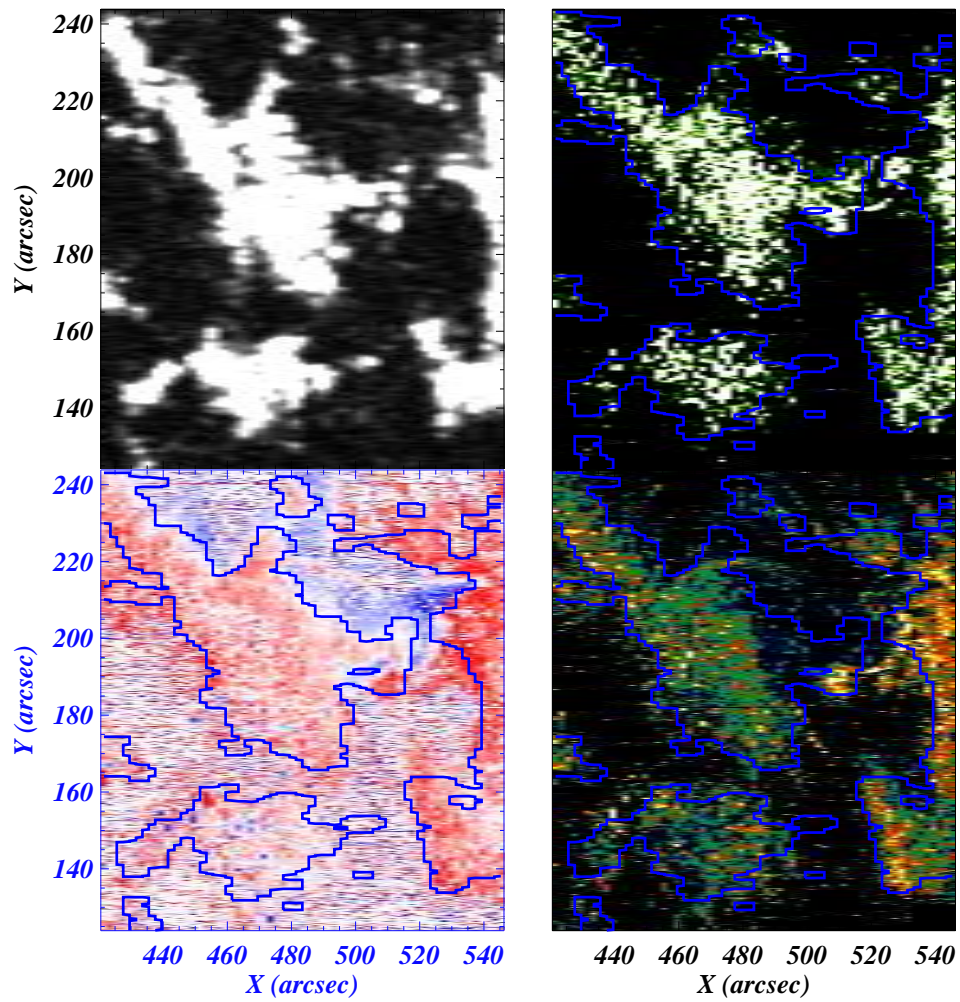
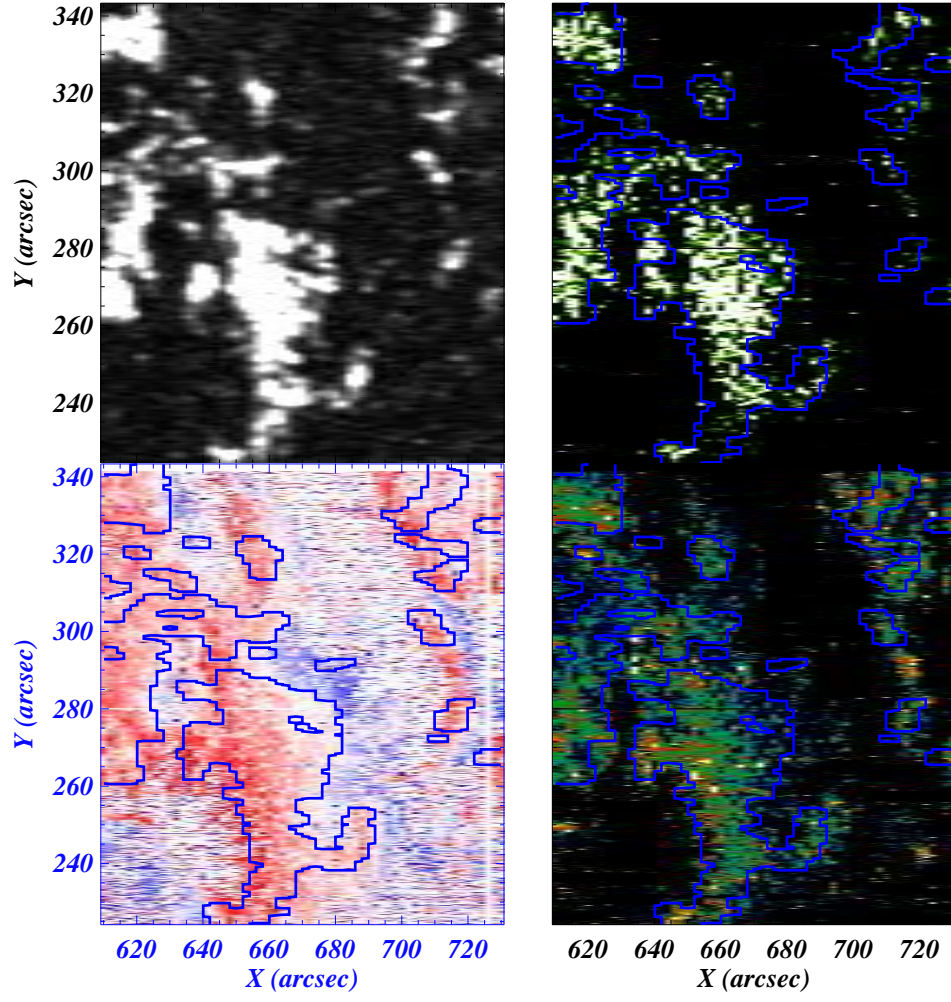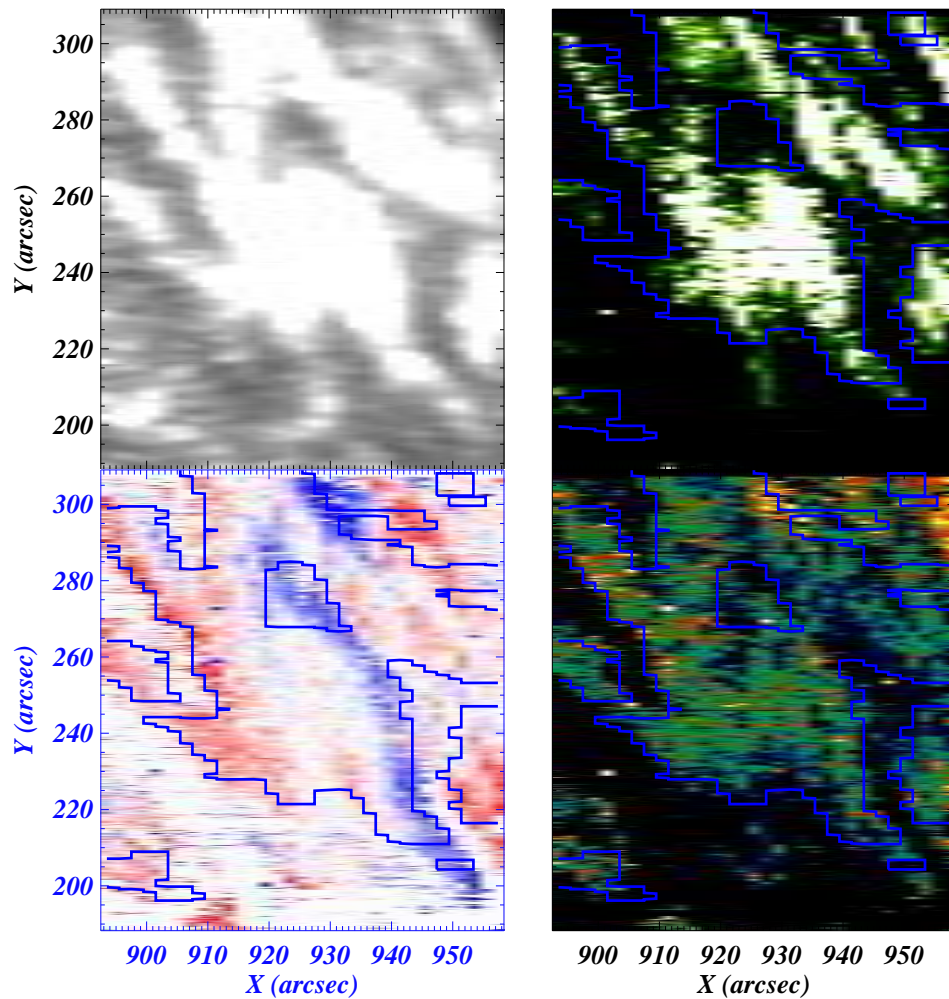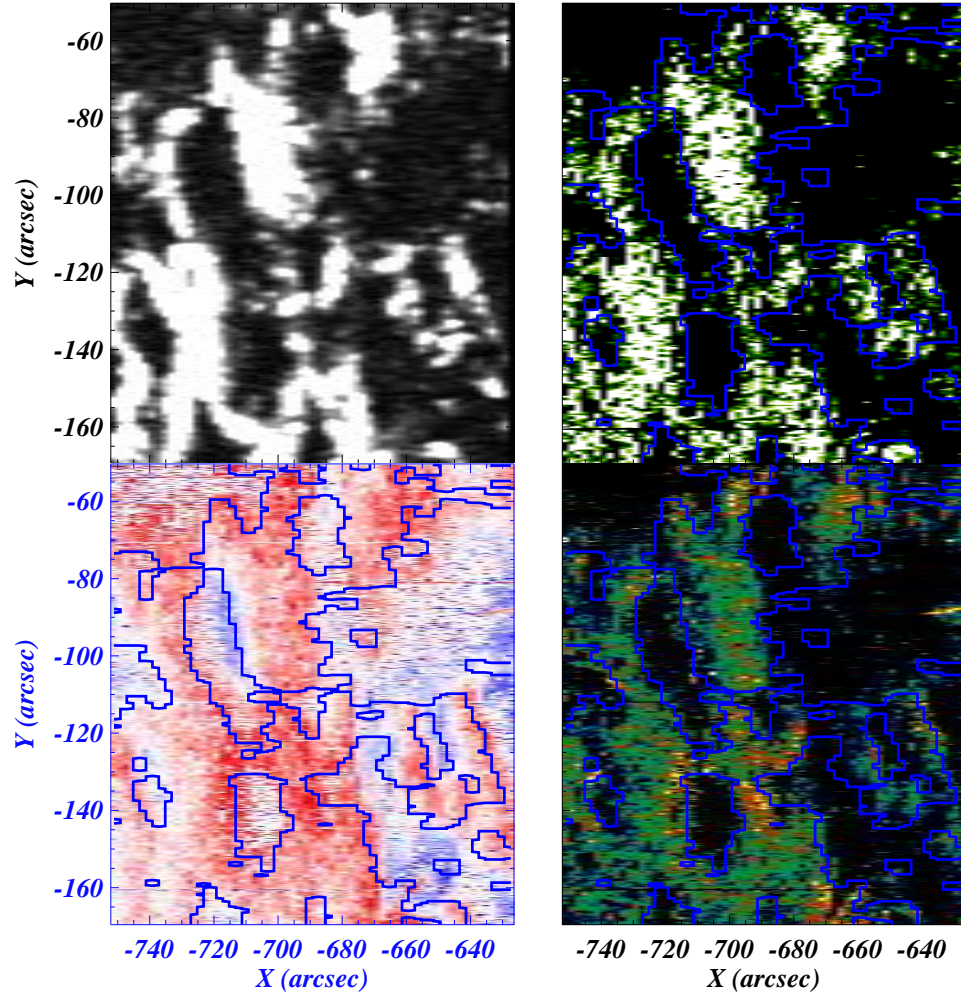**Figure A.3.** Same as panels (b), (c), (d), and (e) of Figure 2 but for 16th December, 2014 observation.
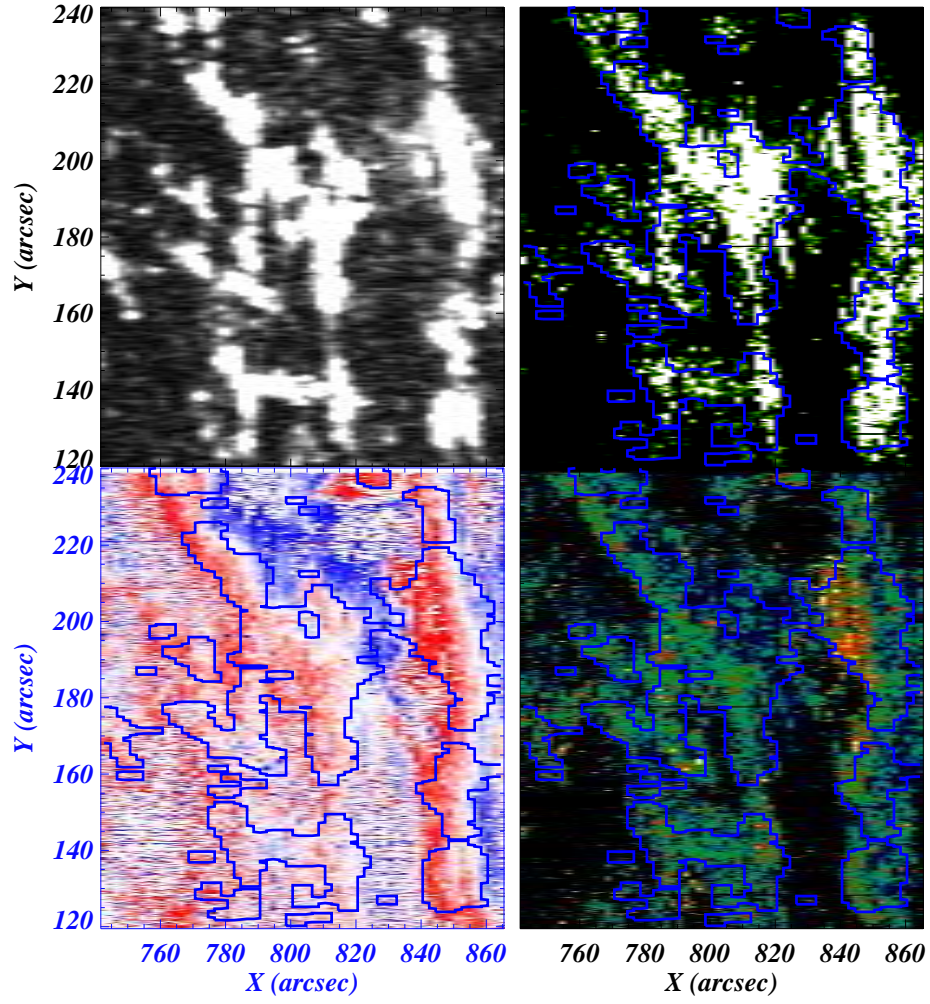
Figure A.4. Same as panels (b), (c), (d), and (e) of Figure 2 but for 18th December, 2014 observation.

Figure A.5. Same as panels (b), (c), (d), and (e) of Figure 2 but for 21th December, 2014 observation.
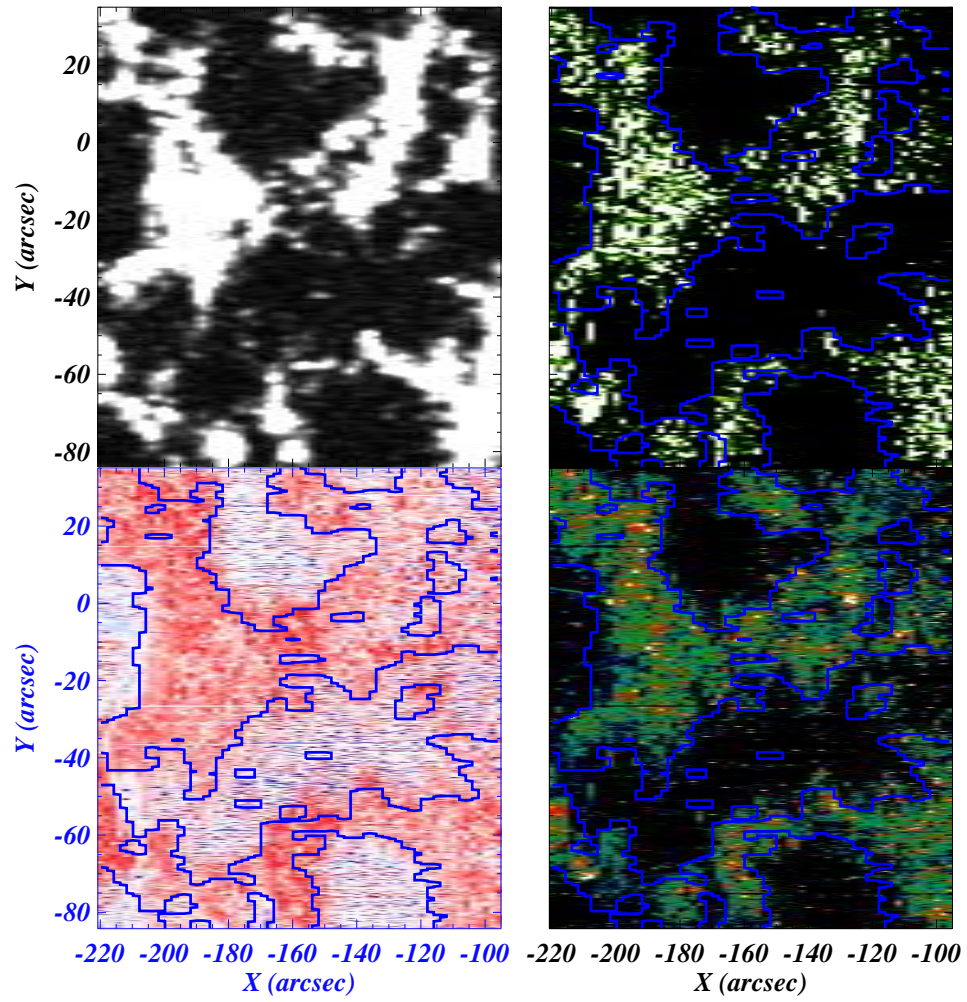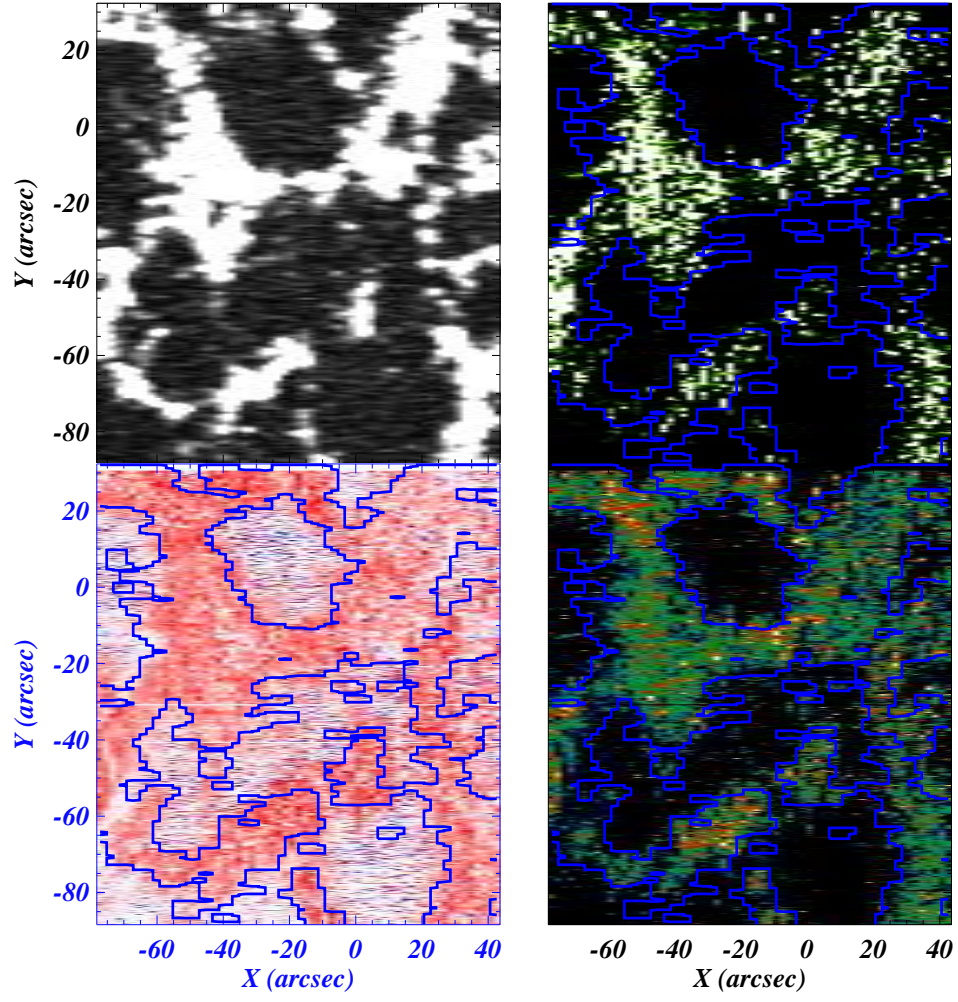
Figure A.6. Same as panels (b), (c), (d), and (e) of Figure 2 but for 12th February, 2015 observation.

Figure A.7. Same as panels (b), (c), (d), and (e) of Figure 2 but for 15th February, 2015 observation. However, it should be noted that we have considered AIA 1600 Å observations (instead of HMI LOS magnetogram) to locate the plage regions. Hence, in this figure, the top-left panel is AIA 1600 Å image, i.e., the AIA 1600 Å raster image is created in the same way as we created magnetogram raster image, see section 3.2.

Figure A.8. Same as panels (b), (c), (d), and (e) of Figure 2 but 21th February, 2015 observation.
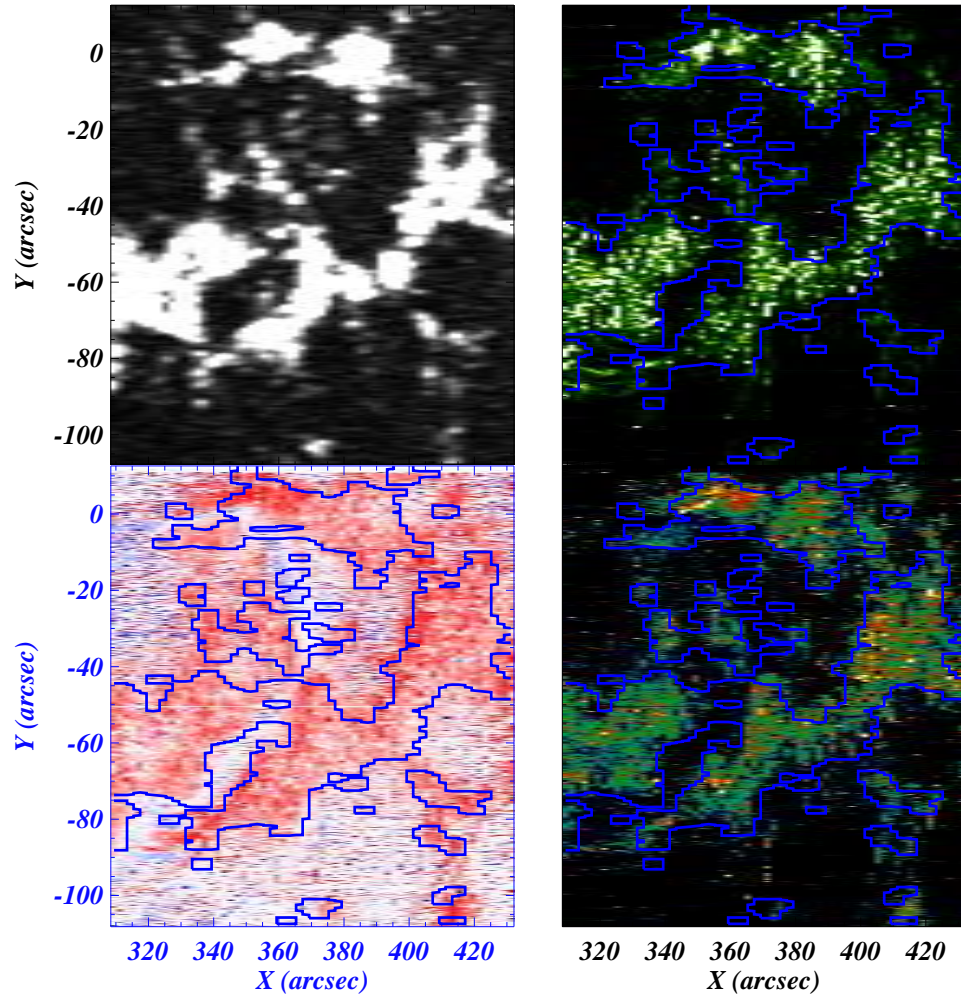
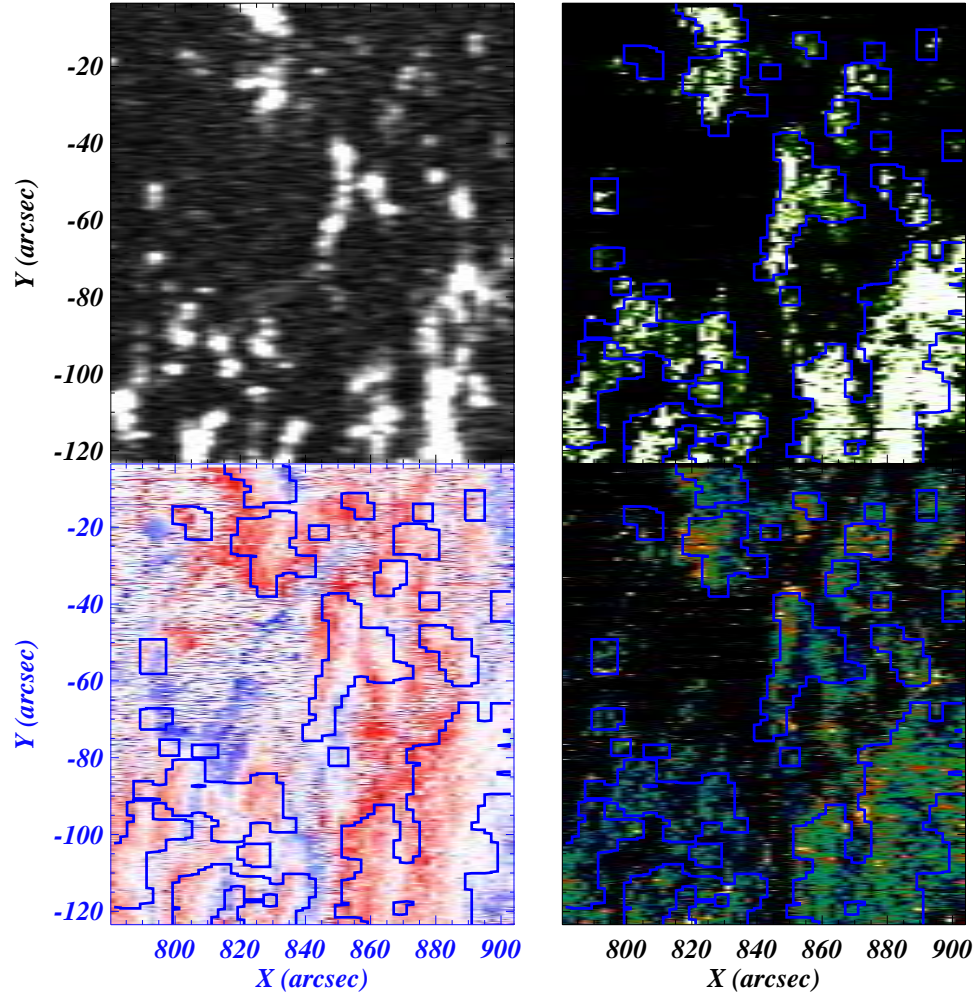**Figure A.9.** Same as panels (b), (c), (d), and (e) of Figure 2 but for 23th February, 2015 observation.

Figure A.10. Same as panels (b), (c), (d), and (e) of Figure 2 but for 24th February 2015 observation.

Figure A.11. Same as panels (b), (c), (d), and (e) of Figure 2 but for 26th February, 2015 observation.

Figure A.12. Same as panels (b), (c), (d), and (e) of Figure 2 but for 01st March, 2015 observation.
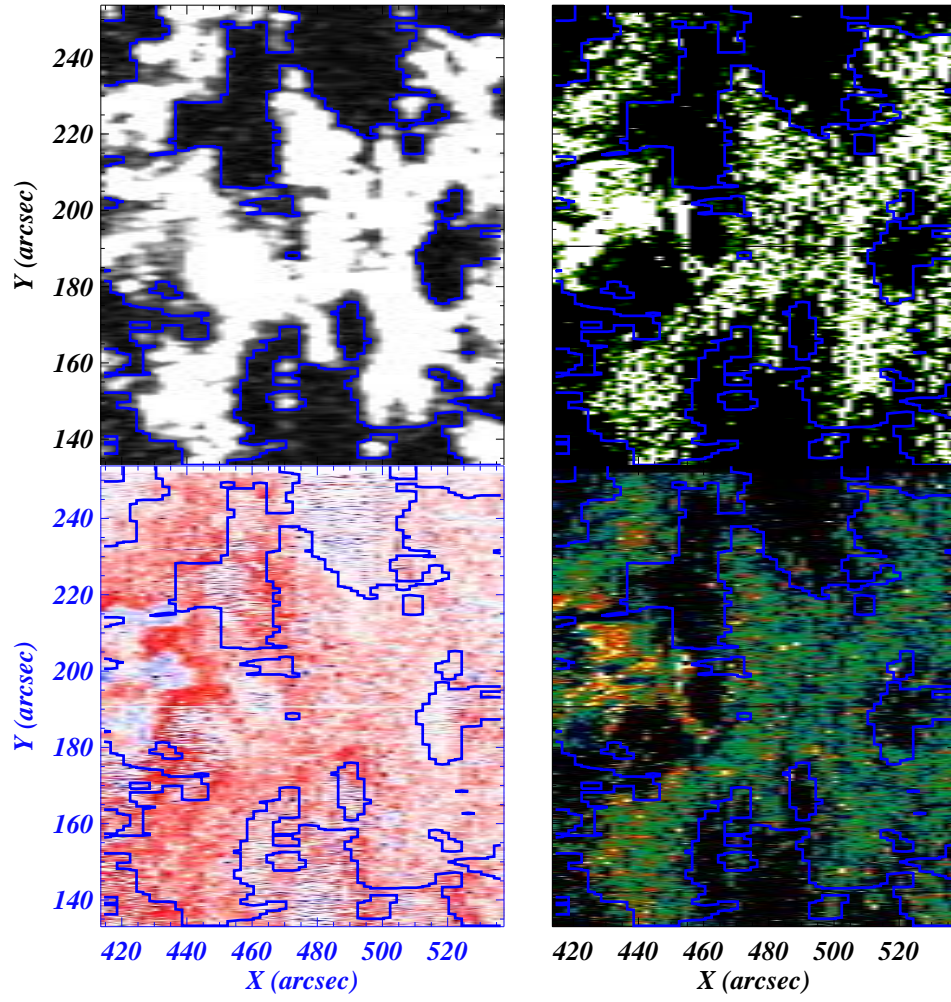
Figure A.13. Same as panels (b), (c), (d), and (e) of Figure 2 but for 03rd March, 2015 observation.
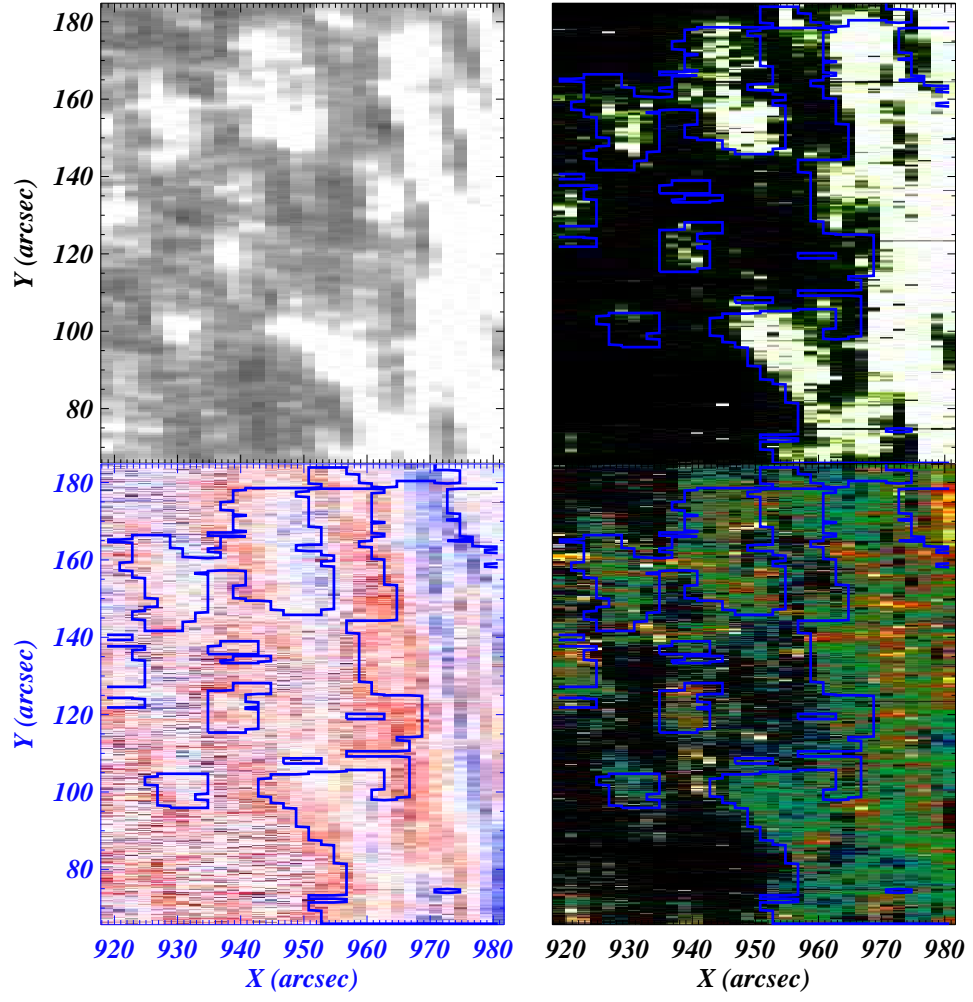
Figure A.14. Same as Figure A.7 but for 08th March, 2015 observation.